1 **Improving 2D-organization of fullerene Langmuir-Schäfer thin films by interaction with**

2 **cellulose nanocrystals**

3 Shadi Sawalha,[a,b] Francesco Milano[c], Maria R. Guascito[d], Simona Bettini[a], Livia Giotta[d]*,

4 Alessandra Operamolla[e,f]*, Tatiana Da Ros[g], Maurizio Prato[g] and Ludovico Valli[d]

5

6 [a] Dipartimento di Ingegneria dell'Innovazione, Università del Salento, S.P. Lecce-Monteroni, I-

7 73100, Lecce, Italy

8 [b] Department of Chemical Engineering, An-Najah National University, P.O. Box 7, Nablus,

9 Palestine

10 [c] CNR-ISPA, Unità Territoriale di Lecce, S.P. Lecce-Monteroni, I-73100, Italy

11 [d] Dipartimento di Scienze e Tecnologie Biologiche e Ambientali, Università del Salento, Università

12 del Salento, S.P. Lecce-Monteroni, I-73100, Lecce, Italy

13 [e] Dipartimento di Chimica, Università degli Studi di Bari Aldo Moro, Via Orabona 4, I-70126 Bari,

14 Italy

15 [f] Present address: Dipartimento di Chimica e Chimica Industriale, Università di Pisa, via Giuseppe

16 Moruzzi 13, I-56124, Pisa, Italy

17 [g] Dipartimento di Scienze Chimiche e Farmaceutiche, Università degli Studi di Trieste, Via

18 Giorgieri 1, I-34127 Trieste, Italy

19

20 * Corresponding author.

21 Tel: +39 0832 299444. E-mail: livia.giotta@unisalento.it (Livia Giotta)

22 Tel: +39 080 5442075. E-mail: alessandra.operamolla@unipi.it (Alessandra Operamolla)

Abstract

Cellulose nanocrystals (CNCs) are renewable, sustainable and biocompatible nanomaterials, which have gained great attention in last years for their potentialities in several fields of application. With their polyelectrolyte behaviour, sulphated CNCs are suitable to produce multilayered architectures with cationic molecules. In this work, we have investigated the ability of anionic CNCs to assist the two-dimensional organization of two cationic fulleropyrrolidines at the air/water interface, leading to hybrid Langmuir-Schäfer films with improved (photo)electrical properties. We demonstrated that CNCs interact with the fulleropyrrolidines at the air/water interface, favouring the assembly of organized hybrid C_{60}/CNC films. The transfer efficiency of Langmuir layers and the morphological regularity of supported films proved to be influenced by the extent of positive charge on the fullerene counterpart. Interestingly, the electrochemical characterization of hybrid films revealed that sulphated nanocellulose strongly improves the electrical properties of organized fullerene layers, by increasing their conductivity and favouring the hydrogen evolution reaction. Moreover, the well-established C_{60} photoactivity proved to be enhanced by CNCs, as demonstrated by the higher intensity of photocurrents. This outstanding nanocellulose impact on fullerene film electrical properties paves the way to the development of more performing C_{60}-based electrochemical devices, able to better exploit the unique properties of carbon nanostructures.

1. Introduction

Several natural materials are object of extensive studies. Among them, cellulose and its crystalline nanostructures [1-3] have attracted great attention for their abundance, low-toxicity [4, 5], high crystallinity [6], outstanding mechanical [7] and thermal properties [8], and optical transparency [9]. Nanocelluloses are renewable, sustainable and biocompatible; they show high aspect ratio, high crystallinity and high tensile modulus (120-145 GPa, comparable to the one of Kevlar) [10, 11]. For this reason, they are often incorporated into nanocomposite materials, with the specific goal of acting as fillers and reinforcing agents [12, 13]. Early reports on the isolation of cellulose nanocrystals (CNCs) from wood pulp by acidic hydrolysis were published by Battista [14] and Rånby *et al*. [15]. However, only recently the intriguing properties of nanocelluloses have given a clearer picture of their potentialities in several fields of application, including manufacturing of nanocomposites [12] and hydrogels [16], drug delivery [17], biocatalyst immobilization [18], biosensors [19] and transparent substrates for optoelectronic devices [20, 21]. Among the various nanocellulose structures, cellulose nanocrystals (CNCs) are defined by the Technical Association of the Pulp and Paper Industry (TAPPI) as crystalline fibres featuring high aspect ratio with a diameter ranging from 5 to 50 nm and length between 100 and 500 nm [22]. CNCs prepared by sulphuric acid hydrolysis of cellulose pulp are negatively charged at pH>1 as a consequence of surface sulphation and form stable colloidal suspensions that can be easily processed [23, 24]. Being polyelectrolytes, sulphated CNCs are amenable to sequential film growth by layer by layer (LbL) assembly [25, 26], to produce multilayered architectures that could, for instance, be used for coating surfaces. In this way, Cranston *et al*. [27] produced structured LbL thin films alternating high aspect ratio nanocrystalline cellulose and the polycation poly(allylamine hydrochloride) on a negatively charged substrate. Likewise, Podsiadlo *et al*. [28] presented anti-reflective coatings based on LbL deposition of nanocelluloses with poly(diallyldimethylammonium chloride). However, a more accurate control of the two-dimensional organization of nanocelluloses is offered by the Langmuir-

Blodgett (LB) or Langmuir-Schäfer (LS) techniques [29-31]. By these methods, floating layers are assembled at the air-water interface and subsequently transferred onto suitable solid supports by either vertical (LB) or horizontal (LS) lifting. Compared to the vertical transfer technique, the horizontal lifting method is faster and more suitable for highly rigid films, whose molecular organization would be perturbed by substrate immersion and withdrawing [32]. Moreover, the multilayers transferred by the Langmuir-Schafer technique present an excellently organised architecture, often referred to as X-type films, with the hydrophobic side of molecules facing the substrate and the hydrophilic side exposed at the surface [33]. The LS method was efficiently applied to the deposition of organic thin films for electronics, a field of application where a fine control over the molecular orientation is crucial in determining the device performances [33-35]. Model 2D-organized thin films of sulphated CNCs were obtained via LB [36] and LS [37] techniques by Habibi *et al.* by spreading a cationic surfactant solution on a CNC aqueous subphase. Since these pioneer reports, no further examples of nanocellulose 2D organization by LB or LS technique appeared in the literature.

Recently, sulphated nanocelluloses have demonstrated high potentialities as dispersing agents for carbon nanomaterials [38-40], like fullerenes, carbon nanotubes and graphene [41]. The surface charge of nanocelluloses probably interacts with the carbon nanomaterials by inducing polarization effects on their sp_2 carbon lattice surface. Thanks to this electrostatic interaction single- and multi-walled carbon nanotubes and reduced graphene oxide could be dispersed in water at different concentrations by interaction with cellulose nanofibers (CNFs) or nanocrystals (CNCs) [38]. The surface sulphation of CNCs was responsible for the surface charge of the aggregates and the stability in water of relevant dispersions. Carbon nanomaterials are suitable candidates for a number of applications in the field of electronics and optoelectronics and their organization in 2D ordered films by LS techniques has been studied aiming at the development of different functional materials [42-45]. In particular, fullerene derivatives display outstanding electron acceptor properties [46]

and, in association with donor molecules, can participate in photoinduced electron transfer processes [47], which represent the triggering step in photovoltaic energy production [48]. Nevertheless, photoactive layers based on the sole fullerene material in absence of donor molecules have also been reported [49]. In general, wet processing, as water processing, may be detrimental for 2D organization of C_{60}-based materials, due to the high hydrophobic character of the fullerene cages that tend to crystallize into large aggregates, compromising the photoresponse of the active layers [50]. Likewise, the electrochemical properties of fullerene layers are strongly affected by grain size and film homogeneity [51,52]. Solutions were already proposed, synthesizing properly functionalized fullerene derivatives [53], some of which are amphiphilic [54] and suitable for layer-by-layer deposition. In the work by Sgobba *et al.* [44], fulleropyrrolidines bearing polar hydrophilic head groups were prepared to enable their LS deposition. The polar portions were introduced by covalent functionalization of the carbon cage, leading to the formation of fulleropyrrolidines with an N-terminating oxyethylene chain. The presence of this appendage minimizes the attractive strong intermolecular π-π interactions between fullerene cages via steric hindrance. Moreover, being positively charged, these materials are less prone to aggregation also because of the electrostatic repulsion between the ammonium and/or pyrrolidinium moieties. The electrostatic coulomb interactions, established at the air-water interface between cationic fullerene derivatives and anionic porphyrins dissolved in the water subphase, were exploited to deposit oriented and ordered monolayer dyad films. The hybrid layers, transferred via the Langmuir-Schäfer method, yielded high-quality, robust, and photoactive thin films with photoconversion efficiency enhanced by increased transfer pressures [44].

Further examples of hybrid Langmuir-Schäfer films with (photo)electrochemical activity have been reported [55,56]. In general, the enhancement of photoactivity represents a big challenge for scientists due to the clear benefits of using light as driving force for a number of applications such as electricity production, pollutant degradation, fuel production, CO_2 capture, chemical synthesis,

etc. In particular, new photocatalytic and photo-electrocatalytic systems have been recently proposed for emerging applications [57-62]. Despite this, very few examples of nanocomposites consisting of nanocellulose and fullerenes have been reported so far, mainly based on direct bioconjugation rather than finely controlled self-assembly techniques and with applications limited to the field of biotechnology and medicine [63,64]. This research aspect remains rather unexplored, in spite composites of nanocellulose with carbon nanotubes, nanodots, or graphene have appeared with interesting applications in the fields of conductive paper [38], materials for charge storage devices [20] and emitters of circularly polarized light [40].

Considering the potentialities shown by sulphated CNCs as dispersing and stabilizing agents for carbon nanomaterials, they represent the ideal candidate to interact with the positively charged fulleropyrrolidines, in consideration of their negative charge, excellent dispersibility in water, sustainability, high specific surface area and high thermal and mechanical stability. In addition, their hydrophilic surface and high specific surface area make them excellent mediators with a water environment. Therefore, in this work, we used cellulose nanocrystals, isolated from Avicel by sulphuric acid hydrolysis [65], for improving the 2D organization of LS films of fullerene derivatives. First, we employed the same fullerene derivatives described by Sgobba *et al*. [44] to assemble at the air/water interface the cellulose nanocrystals suspended in the subphase. Afterwards, we deposited the resulting hybrid films by horizontal lifting onto suitable substrates and investigated the role of CNCs in enhancing the (photo)electrochemical performances of C_{60} films in aqueous environment.
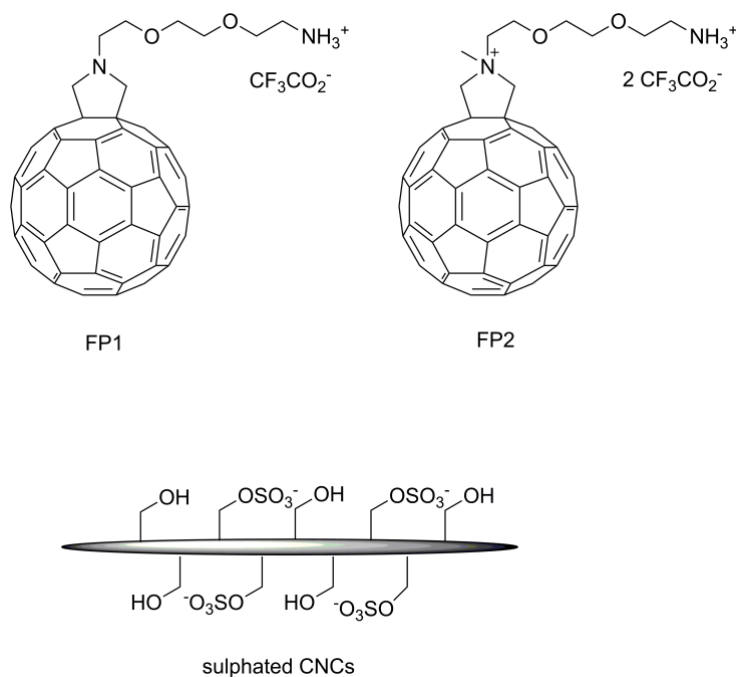
Figure 1. Structures of the materials used in the present work: fullerene derivatives **FP1** and **FP2** and sulphated cellulose nanocrystals (CNCs).

2. Experimental

2.1 Synthetic procedures

2.1.1 Fullerene derivatives: The fullerene derivatives **FP1** and **FP2** (whose structures are reported in Figure 1) have been prepared according to published synthetic protocols [66]. As previously mentioned, these fulleropyrrolidines are the same reported in [44], except for the counterion, which is trifluoroacetate in our case instead of chloride.

2.1.2 Cellulose nanocrystals (CNCs): Avicel PH-101 was used as starting material for nanocrystalline cellulose isolation. Sonication of water suspensions was carried out with a Bransson Sonifier 250. 40 mL of deionized water were introduced in a 250 mL three necked round-bottom flask equipped with a water condenser and a mechanical stirrer. Then, the flask was cooled in an ice bath and 40 mL of concentrated H_2SO_4 were added. After that, 5 g of Avicel PH-101 were added

and the suspension was warmed to 45°C for 80 minutes. The system was cooled to room temperature and the mixture was transferred to polypropylene centrifugation tubes. Centrifugation at 1300 rcf for 10 minutes was repeated replacing the supernatant solution with deionized water until the pH was approximately 1. Then the precipitate was suspended in deionized water and dialyzed against distilled water until neutrality, using a cellulose nitrate membrane with a molecular weight cut-off of 12400 Da. The resulting suspension was sonicated with the aid of a tip sonicator (power 40 W, duty cycle 60%, time 10 mins) and transferred into polypropylene centrifugation tubes. The suspension was centrifuged at 1300 rcf for 10 minutes. The supernatant solution contained nanocellulose rods with length 280±70 nm, width 10±2 nm and aspect ratio 28, detected by AFM [62], with a total concentration of 18 mg/mL, which was suitably diluted for the experiments.

2.2 Langmuir isotherms and Langmuir-Schäfer deposition

Chloroform (Fluka, HPLC grade) and dimethylsulfoxide (Fluka, GC grade) were used as solvents for the spreading solutions of fullerene derivatives **FP1** and **FP2**. For both compounds a 0.145 mg/ml solution was obtained after dissolving fullerene in a few drops of dimethylsulfoxide and then adding chloroform up to the required total volume. These solutions can be pondered as colloidal suspensions due to the incomplete solubilisation of fulleropyrrolidine colloidal particles in the spreading solvent [44]. Langmuir isotherms were recorded by a NIMA 601BAM trough with a 450 cm^2 surface area. Ultrapure water (resistivity larger than 18 MΩ cm) from a Milli-Q system was employed as control subphase and for the preparation of CNC-supplemented subphases. For this purpose, the starting 18 mg/ml CNC suspension was diluted to 0.036 mg/ml, representing the minimal concentration able to induce a clear and reproducible effect on fulleropyrrolidine Langmuir layer properties. A 200 μl aliquot of the fulleropyrrolidine solutions was spread at the air/water

interface on both CNC-free and CNC-supplemented subphases. After solvent evaporation, the floating film was compressed continuously at a speed of 7 cm^2/min while the surface pressure was monitored by a Wilhelmy balance, thus allowing the acquisition of the Langmuir isotherm of the sample.

The layers assembled at the air/water interface were transferred by the Langmuir-Schäfer deposition technique, which is performed by stamping the substrate on the floating film and lifting it upwards very slowly. The wet transferred films were then dried gently by N$_2$ gas. Multilayers were deposited by repetitive stamping of substrates on different areas of the floating layer, using a suitable Teflon mask. During the transfer a surface pressure of 18 mN/m was typically used. Deposition was carried out on clean quartz slides for AFM and on glass/ITO substrates for FTIR characterization and electrochemical measurements. Prior to the transfer (deposition) all substrates were rendered hydrophobic by exposing them overnight to vapours of 1,1,1,6,6,6-hexamethyldisilazane in a desiccator.

2.3 Brewster Angle Microscopy

Brewster angle microscopy (BAM) analysis [67] was carried out using the same NIMA 601BAM apparatus, at a compression speed of 7 cm^2/min. BAM images were acquired at different surface pressures using a NFT BAM 2plus system with a lateral resolution of 2 µm.

2.4 Infrared Spectroscopy

Mid-infrared spectra were acquired in wavenumber range 4000-400 cm^{-1} at 4 cm^{-1} resolution with a Perkin-Elmer Spectrum One FTIR spectrometer equipped with a DTGS detector [68]. An ATR horizontal sampling apparatus was employed for the analysis of fullerene and CNC starting materials, which were analysed as powders (**FP1** and **FP2**) and as drop cast film (CNCs). The internal reflection element (IRE) was a three bounce 4 mm diameter diamond microprism mounted into a stainless-steel plate (Smiths technologies, former SensIR

technologies). Spectra of LS films deposited on ITO/glass slides were acquired by a multireflection accessory suitably designed for thin film analysis (AmplifIR, SensIR technologies).

2.5 AFM measurements

Atomic force microscopy topographies were taken using a Park XE-100 SPM system microscope. Images were acquired in non-contact mode using tips (Type PPP-NCHR) on a cantilever of 125 µm length, about 330 kHz resonance frequency, 42 N m^{-1} nominal force constant and <10 nm guaranteed tip curvature radius. Surface areas were sampled with a scan rate of 1 Hz. Topographies were analysed using the software XEI (Park System Corporation, version 1.8.0).

2.6 Electrochemical measurements

Electrochemical experiments were carried out by means of a µStat400 portable electrochemical sensor interface workstation (DropSens, Spain) controlled by computer. A three-electrode configuration with an Ag/AgCl reference electrode and a platinum wire counter electrode was employed. The working electrode (WE) was an ITO-coated glass slide where **FP1** layers, assembled either on pure water or on a CNC subphase, were deposited by the LS technique. A 90 mM potassium phosphate buffer solution at pH 7.0 was employed as electrolyte medium. The electrochemical measurements were conducted without addition of any redox mediators and in aerobic conditions. Linear sweep voltammetry (LSV) measurements were conducted sweeping the potential from 0 to -500 mV at 50 mV/s scan rate. In order to investigate the electrochemical photo-response, analogous LSV traces were recorded under illumination. For this purpose, the light source was a 150 W quartz tungsten halogen lamp placed at 5 cm from the surface of the WE. Photo-chronoamperometry traces

1 were recorded at controlled WE potential, alternating darkness and light periods, using the

2 same illumination system.

3. Results and discussion

3.1 Characterization of fullerene/CNC layers at the air/water interface

3.1.1 Langmuir isotherms. The Langmuir isotherms for both **FP1** and **FP2** recorded on a pure water subphase and on an aqueous subphase containing 0.036 mg/mL CNCs are reported in Figure 2. The value of the limiting area per molecule was obtained by extrapolating the steep ascending portion of the Langmuir curve to surface pressure π=0 mN/m. For **FP1**, the found limiting area per molecule was about 75 Å^2, lower than the theoretical value of an ideal fullerene monolayer, equal to 86.6 Å_2 [44]. This low value agrees with the establishment of intermolecular attractive π-π interactions between fullerene moieties resulting in stable 3D van der Waals aggregates with cohesive energy larger than 30 kcal/mol [44]. The comparison between curves in Figure 2a indicates that the presence of cellulose nanocrystals in the subphase leads to modifications of the Langmuir isotherm, with a marked shift to higher limiting area value of 112 Å_2. This can be ascribed to the attractive electrostatic interactions established between the positively charged **FP1** and the negatively charged CNCs. The CNCs dispersed in the subphase may affect the limiting area value of **FP1** by either penetrating the forming film or by inhibiting the 3D aggregation of fullerene moieties, enhancing the 2D character of the layer. The same preliminary evaluation via Langmuir isotherms analysis was performed also for **FP2**, on both pure water and 0.036 mg/ml CNC solution subphase. The corresponding isotherms are shown in the Figure 2b. As expected, **FP2** interacts with cellulose nanocrystals producing a shift in the limiting area from 95 Å_2 to 125 Å_2 and this dramatic increase could be attributed again to the presence in the floating film of cellulose nanocrystals, whose electrostatic interaction with **FP2** is strengthened by the double positive charge.

1
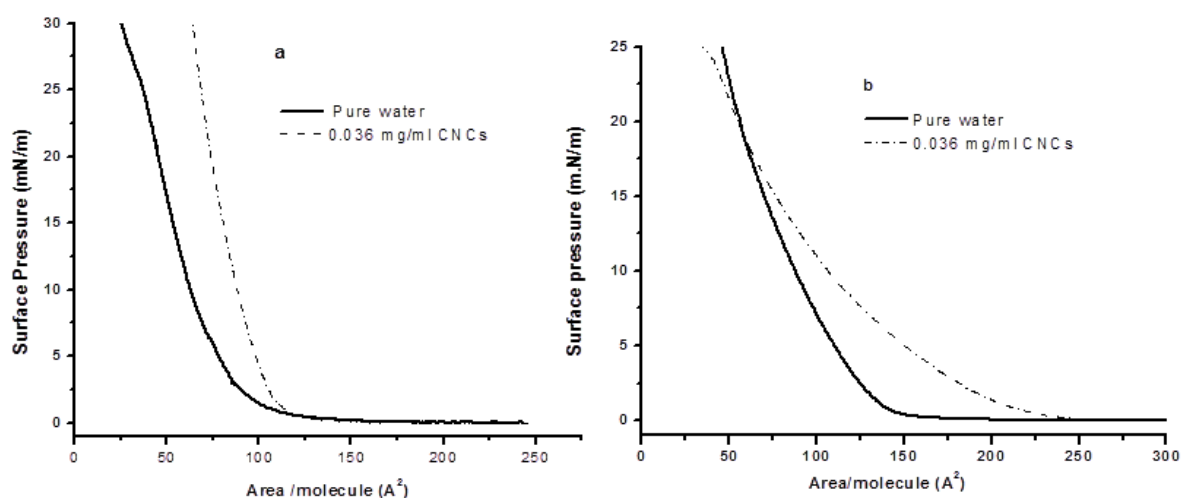
Figure 2. Langmuir isotherms recorded for **FP1** (a) and **FP2** (b) spread on a pure water subphase (continuous

lines) and on a 0.036 mg/ml CNC aqueous suspension (dashed lines).

4

5 **3.1.2 Brewster Angle Microscopy.** Brewster Angle Microscopy (BAM) measurements were

acquired on the floating films at the air/water interface for both **FP1** and **FP2** interacting

with a pure water or a 0.036 mg/ml CNC subphase. The BAM micrographs, shown in

Figures 3 and 4 respectively, allow observing the progress of floating film formation,

enlightening morphology changes occurring during the compression. **FP1** and **FP2** films

appear heterogeneous, presenting both two-dimensional and three-dimensional features. The

bright spots in the micrographs can be assigned to large fulleropyrrolidines 3D aggregates,

while the dark background, which turns to grey at higher surface pressures, represents the

monolayer, whose density is controlled by surface pressures.
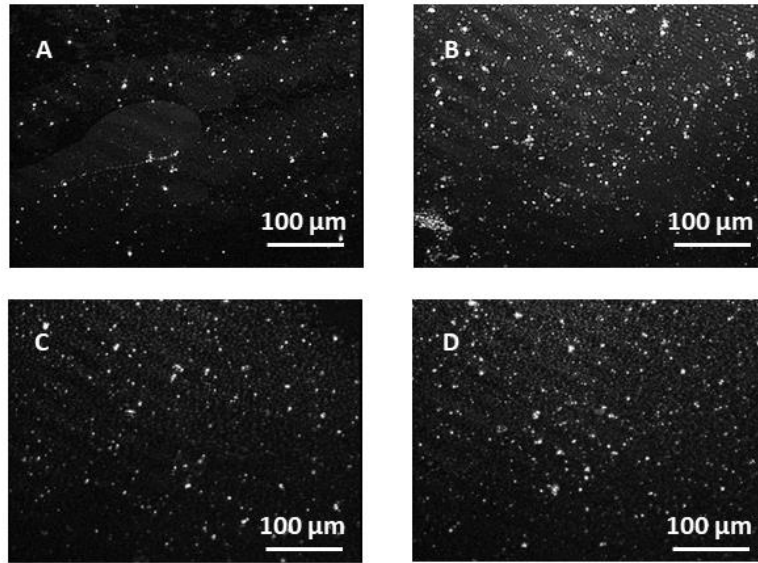
Figure 3. BAM micrographs of floating layers of **FP1** on a pure water subphase (A, B) and on an aqueous subphase containing CNCs at a concentration of 0.036 mg/mL (C, D). Micrographs A and C were acquired at 11 mN/m surface pressure, while micrographs B and D were acquired at 18 mN/m, representing the target pressure employed for film transfer.
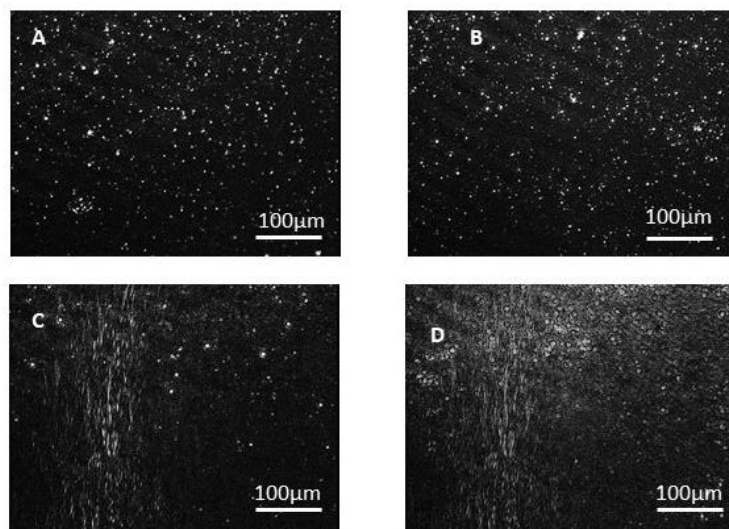
Figure 4. BAM micrographs of a layer of **FP2** on a pure water subphase (A, B) and on an aqueous subphase containing CNCs 0.036 mg/mL (C, D). Micrographs A and C were acquired at 7 mN/m surface pressure, while micrographs B and D were acquired at 18 mN/m, representing the target pressure employed for film transfer.

13

As observed on the microscopic scale accessible with this technique (100 μm scale bar), CNCs seem to have negligible influence on the amount and size of fulleropyrrolidine 3D aggregates. Actually, these characteristic floating aggregates appear as soon as solvent evaporates at zero surface pressure and likely represent colloidal particles of unsolubilized fulleropyrrolidine, whose amount at the air-water interface is not expected to depend on the subphase composition. The tendency to form this kind of aggregates was shown in a previous investigation [44] and explained on the basis of the limited solubility of **FP1** and **FP2** in the spreading solvent (CHCl$_3$). Even the addition of a minimal amount of dimethylsulfoxide was not sufficient to achieve a complete dissolution of solid particles. Therefore, our BAM investigation demonstrated that CNCs dispersed in the subphase are not able to modify pre-existing fullerene aggregates (bright spots), suggesting that Langmuir isotherms modification arises from the CNC influence on the organization of the Langmuir layer, appearing homogenous at the microscale as a black/grey background, formed by fulleropyrrolidine molecules spread in non-aggregated form at the air/water interface. Following these considerations, a more in-deep morphological investigation was necessary in order to elucidate the effect of the charged cellulose nanocrystals on the fullerene film organisation (or the reciprocal effect) at the nanoscale.

3.2 Characterization of fullerene/CNC layers deposited onto solid substrates

3.2.1 AFM measurements. The surface topographies of the LS hybrid films were acquired by atomic force microscopy (AFM). AFM is a powerful tool to follow modifications in the aggregation pattern and was very useful to gain information on the morphology of assembled films. The floating layers were horizontally transferred on quartz substrates with the fullerene layer in contact with the substrate surface and the nanocellulose exposed on

top. Hence, differently from BAM microscopy that provided more information about the morphology of fullerene layers at the microscale, the AFM permitted to evaluate the organization of CNCs assisted by the two fullerene derivatives and the overall quality of the hybrid films at the nanoscale. The 2.5 x 2.5 μm^2 topographies were collected (Figure 5; for wider topographies, see also Appendix A, Figure S1). The topography for the sole **FP1** Langmuir-Schäfer film is shown in Figure 5a. **FP1** characteristically exhibits small crystallites (few tens of nanometers in diameter), which aggregate in a homogeneous film-like structure. Bigger area topographies (see Appendix A) revealed an uncomplete surface coverage for **FP1**. The AFM topography acquired on drop cast CNC films, shown in Figure 5d, certified the presence of rod-like crystals. In a previous work, it was demonstrated that the average rod length was 280±70 nm, with a diameter of 10±2 nm [65].
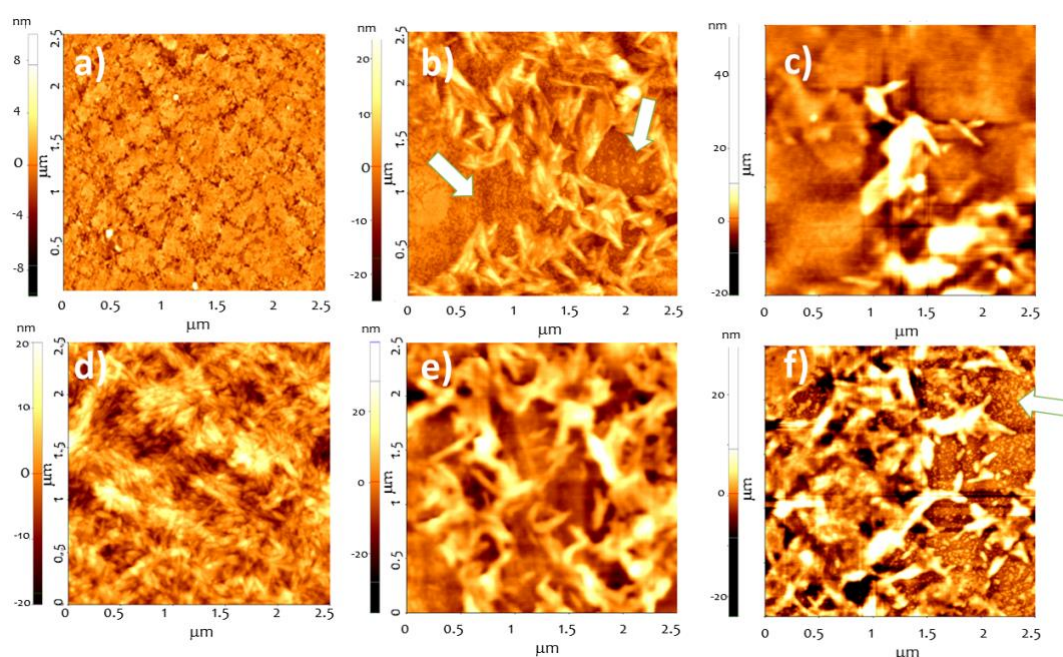
Figure 5. 2.5 x 2.5 μm^2 AFM non-contact topographies of thin films, deposited on quartz slides, of: a) **FP1** single transfer LS film; b) **FP1**/CNC single transfer LS film; c) **FP2**/CNC single transfer LS film; d) drop cast thin film of CNCs; e) **FP1**/CNC triple transfer LS film; f) **FP2**/CNC triple transfer LS film. White arrows in panels b-f evidence areas with uncovered fullerene underlayer.

CNCs typically aggregate by their longitudinal dimension, thanks to the establishment of H-bond interactions. However, the poor amphiphilic nature of CNCs [69] requires a second material to assist their strict organization in two-dimensional patterns by LS technique. Figure 5 shows the surface morphology for the two fullerene/CNC LS films both after single (5b, c) and triple (5e, f) transfer on quartz. The best situation is the one described in topographies 5b and d, relative to LS films formed by **FP1** and cellulose nanocrystals. In the conditions under investigation, **FP1** proved to be very effective in assisting the two-dimensional self-assembling of CNCs at the interface: in particular, topography b (**FP1**/CNC single transfer LS film) reveals the presence of a thin 2D layer of cellulose nanocrystals connected, as expected, by their longitudinal dimension. The surface coverage is however uncomplete, revealing areas with uncovered fullerene underlayer (see also Figure S1). After three horizontal transfers (Fig. 5e), instead, the surface coverage is much improved, and the film keeps on exposing the CNC layer to air, revealing a certain order among the hybrid bilayers.

Conversely, the **FP2** proved to direct the 2D organization of CNCs in supported films less efficiently than **FP1**. Irregular aggregates were revealed in the topography corresponding to a single LS transfer of **FP2** with CNCs (Fig. 5c), with a very patchy coverage of the surface. Consequently, the hybrid film left a wide uncovered glass surface. After three LS transfers the situation slightly improved, with areas containing hybrid aggregates of fulleropyrrolidine and nanocrystals and areas where only small globular aggregates, presumably of **FP2**, were present. This behaviour is not surprising, considering that cellulose nanomaterials are very effective dispersing agents for charged carbon nanomaterials. It is possible to envision that the higher surface charge of **FP2** favours the formation of colloidal dispersions of **FP2** and CNCs, which interfere with the desired 2D ordered organization that the LS technique should allow to achieve [38]. The trade-off of this phenomenon is represented by the use of

the single charged fulleropyrrolidine, allowing two-dimensional organization of both nanomaterials.

3.2.2 FTIR spectroscopy measurements. As a preliminary measurement, the three starting materials were analysed by FTIR spectroscopy using an ATR sampling apparatus. The relevant ATR-FTIR spectra are shown in Figure S2. The spectrum of cellulose nanocrystals (trace A in Figure S2) shows the typical absorption profile found for samples mainly composed of cellulose I. The strong absorption band corresponding to OH stretching vibrations, as arising from intramolecular hydrogen bonds [70], is centred at 3342 cm^{-1}. Multiple bands below 3000 cm^{-1} (2969, 2940 and 2904 cm^{-1}) arise from C-H stretching modes. The band at 1630 cm^{-1} can be attributed to crystallized water, while the intensities of characteristic bands at 1373 cm^{-1} and 2904 cm^{-1} are typical of highly crystalline cellulose materials. The Lateral Order Index (1.11), i.e. the ratio between the "crystallinity" band at 1428 cm^{-1} (symmetric CH$_2$ bending vibration) and the "amorphous" band at 898 cm^{-1} (C-O-C stretching at β 1-4 glycosidic linkages) [71, 72], despite being an underestimated value due to ATR band distortion, is in line with a high crystallinity degree of CNCs. On the other side, the spectra of both fullerene derivative powders (traces B and C in Figure S2) are dominated by intense absorption bands between 1100 and 1300 cm^{-1} arising from the trifluoroacetate counterion (C-F stretches [73]), although the contribution of the fulleropyrrolidine moiety is detectable. In particular, the methylene group stretching vibration signals are well evident in **FP1** powder spectrum at 2953, 2921 and 2851 cm^{-1}. The comparison of **FP1** and **FP**2 spectra with sodium trifluoroacetate spectrum reported in the literature [74] allows assigning to the counterion the intense absorption band at 1675 cm^{-1} (COO$^-$ stretching) and the sharp absorption bands between 700 and 900 cm^{-1}. The higher contribution of trifluoroacetate spectral features in the infrared spectrum of **FP2** powder is in line with the higher counterion content arising from the double fulleropyrrolidine charge.

1 The clear identification of CF_3COO^- spectral features helped to understand, as will be

2 discussed later, the connection between the fate of the counterion and the electrochemical

3 activity of the fullerene derivative **FP1**.
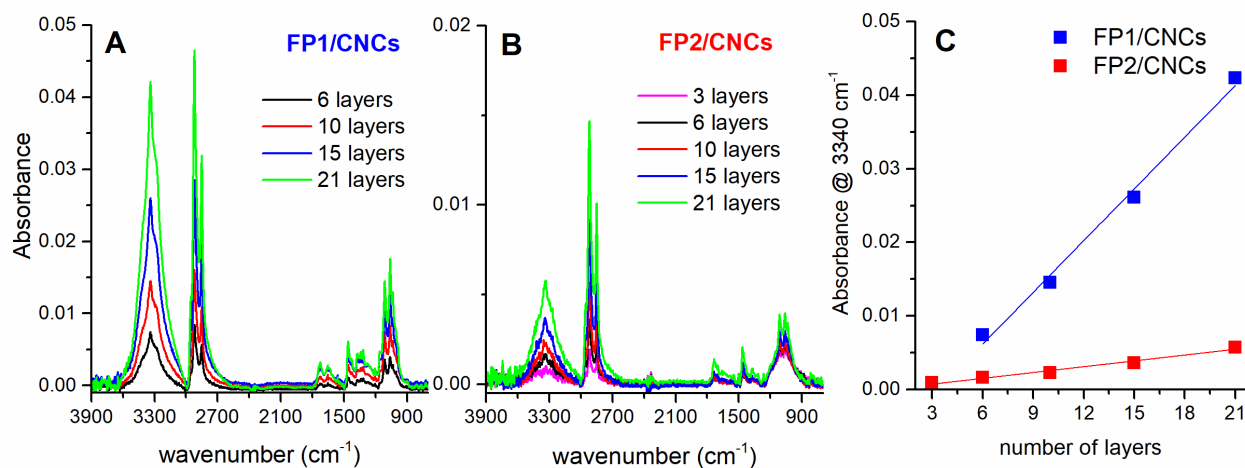
4
5 Figure 6. FTIR spectra acquired in multireflection mode of LS hybrid films resulting from the

6 deposition of multiple layers of **FP1**/CNCs (A) and **FP2**/CNCs (B). Panel C shows the absorbance at

7 3340 cm^{-1} (CNC marker band) as a function of the number of LS runs for both **FP1**/CNC (blue

8 squares) and **FP2**/CNC (red squares) hybrid films, with the relevant linear fitting.

9

10 Hybrid layers of both **FP1**/CNCs and **FP2**/CNCs were transferred onto ITO modified glass

11 at 18 mN/m surface pressure. Since ITO reflects mid-infrared radiation, the films were

12 suitably analysed in multi-reflection mode, which enhances the sensitivity of FTIR

13 spectroscopy and allows to assess the film transfer efficiency by horizontal lifting.

14 Panel A in Figure 6 shows the mid-infrared absorption spectra of the films relevant to the

15 **FP1**/CNC system. The spectra confirmed the presence of CNCs in the hybrid films with

16 their intense absorption bands at 3340 cm^{-1} (O–H stretching) and at 1060 cm^{-1} (C–O

17 stretching). The presence of **FP1** moiety in hybrid films is highlighted by bands at 2952,

18 2919 and 2849 cm^{-1} that can be mainly assigned to C–H stretching vibrations of **FP1**

methylene groups, although cellulose C–H vibrations also contribute to infrared light absorption in this region.

A further spectroscopic evidence of the presence of both components in transferred films was given by the comparison between the absorption profile recorded for a LS film of sole **FP1** and the one corresponding to a hybrid **FP1**/CNC film (Figure S3). The relevant difference spectrum (Figure S3, trace C) shows in fact the infrared absorption pattern of nanocellulose. It is noteworthy the dramatic decrease of trifluoroacetate spectral features in the FTIR spectrum of **FP1** LS film (Figure S3, trace B), as arises from comparison with the relevant powder spectrum (Figure S2, trace B). This finding indicates that most of CF_3COO^- counterions of **FP1** are lost once its floating layer is compressed on a pure water subphase and transferred to the substrate. Being anion exchange processes ruled out in pure water, this phenomenon is consistent with the perturbation of acid-base equilibria at the air/water interface, which strongly affect the pKa value of acidic groups favouring the neutral form [75]. Hence, based on our FTIR data, we can argue that, in absence of CNCs dispersed in the subphase, the terminal ammonium group of **FP1** undergoes significant deprotonation at the air-water interface, leading to LS films with a low ionic character.

The intensity of mid-infrared spectra relevant to **FP1**/CNC films (Figure 6, panel A) increases with the number of horizontal lifts achieved, while maintaining the same qualitative pattern. This finding indicates that specific interactions between CNCs and **FP1** floating layer result in organized hybrid films with a well-defined stoichiometry, which is retained during the transfer process. The efficiency of the LS deposition method for this two-component system was confirmed by the linear dependence of the absorbance at 3340 cm^{-1} on the number of transferred **FP1**/CNC layers, as shown in panel C (blue squares) of Figure 6.

Panel B in Figure 6 shows the mid-infrared absorption spectra relevant to multiple layers of **FP2**/CNC hybrid films deposited at the same surface pressure (18 mN/m). In agreement with AFM data, in this case the absorption intensity was significantly lower, confirming the lower compactness and quality of transferred films. Although a linear dependence between the absorbance at 3340 cm^{-1} and the number of LS runs was observed, the smaller slope of the relevant fitting line clearly indicates that the amount of transferred material onto the ITO/glass slide was much smaller than one achieved in the case of **FP1**/CNC hybrid films. Moreover, the ratio between C-H stretching band at 2919 cm^{-1} and O-H stretching band at 3340 cm^{-1} was higher in **FP2**/CNC FTIR spectra than in **FP1**/CNC spectra. Being the absorption at 3340 cm^{-1} a marker signal for nanocellulose, this result is consistent with a lower CNC content in **FP2**/CNC hybrid films with respect to the fullerene counterpart. These findings suggest that, though fairly assembled at the air/water interface, as demonstrated by isotherm modification and BAM images, **FP2**/CNC hybrid layers are transferred horizontally onto the solid support with a very poor efficiency, leading to low quality LS films. The more pronounced hydrophilicity of **FP2**/CNC hybrid layers likely plays a role in weakening the adhesion of the Langmuir film to the solid support, favouring the loss of material by dispersion in the aqueous phase.

The low contribution of CF$_3$COO$^-$ signals in **FP1/**CNC and **FP2/**CNC hybrid film spectra, as arisen from the comparison with the spectra acquired from the powders (Figure S2, traces B and C), can be mainly ascribed to the electrostatic interaction with CNCs, which replace most of trifluoroacetate counterions. The polyelectrolyte behaviour of nanocellulose thus stabilizes the positive charge on terminal -NH$_3^+$ groups, making negligible the deprotonation processes at the air water-interface and enhancing the ionic character of LS hybrid films.

3.3 Photo-electrochemical activity of FP1/CNC films

1 Since AFM and FTIR data clearly demonstrated the better quality of **FP1**/CNC LS films, the

2 subsequent investigation was focussed on the functional properties of layers assembled with

3 **FP1**. In particular, the photo-electrochemical activity of both **FP1** and **FP1**/CNC hybrid

4 films was assessed and compared, in order to unveil a possible role of CNCs in improving

5 (or worsening) the photo-electrochemical performances of fullerene-based materials.

6 Nanocelluloses notably display good wettability in various electrolytes and stability over a

7 wide potential window [76], characteristics that make them highly compatible with

8 electrochemical studies. Furthermore, the CNCs offer a high specific surface area, due to

9 their nanometric dimensions. This creates opportunities for the electrolyte solution of

10 establishing percolation paths across the binary films that we prepared, which could be

11 beneficial to the photo-electrochemical response of **FP1**.

12 All electrochemical measurements were conducted immersing a 0.4 cm^2 portion of the WE

13 electrode into the electrolyte medium. The WE was an ITO/glass slide where 5 layers of

14 either **FP1** or **FP1**/CNCs were deposited by the Langmuir-Schäfer approach described

15 previously.

16 The linear sweep voltammetry (LSV) measurements, acquired by sweeping the potential

17 from 0.00 mV to -500 mV vs Ag/AgCl at 50 mVs^{-1} scan rate, are shown in Figure 7. The

18 voltammetric curves are relevant to the bare ITO working electrode (black line) and to the

19 ITO electrodes modified with **FP1** (blue line) and **FP1/CNC**s (red line). Since no redox

20 active species were present into the aerobic electrolyte medium, faradaic currents could be

21 ascribed only to the oxygen reduction reaction (ORR) or to the hydrogen evolution reaction

22 (HER). The bare ITO electrode showed low cathodic current densities, revealing a negligible

23 hydrogen evolution reaction (HER) rate. The charge transfer through the ITO/electrolyte

24 interface allowing HER is notably not favoured, considering the low H$^+$ adsorption on the

1 ITO surface [77]. On the other side, the small shoulder at -175 mV (see inset in Figure 8)

2 could be attributed to ORR, made feasible on ITO by the aerobic electrolyte medium.
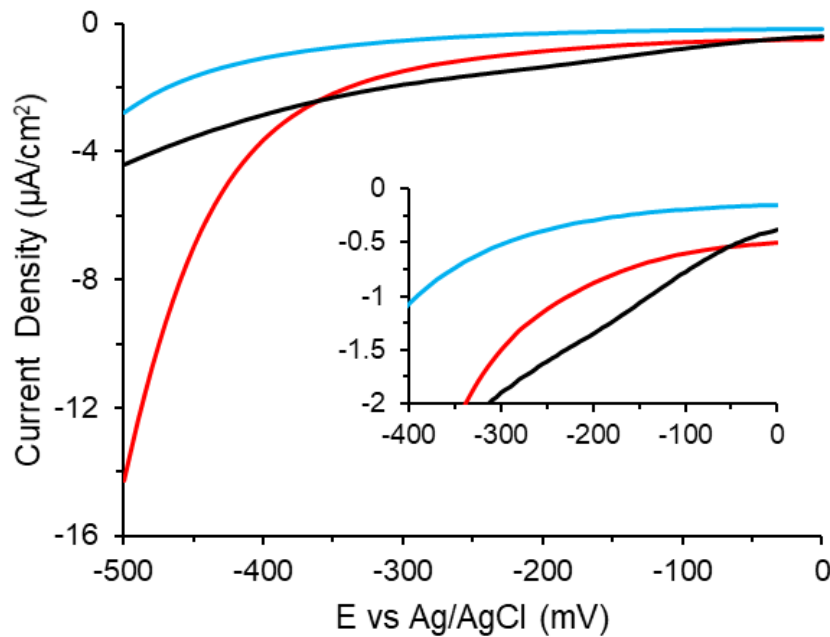
3

4 Figure 7. LSV traces obtained sweeping the potential from 0 to -500 mV *vs* Ag/AgCl in a three-electrode

5 electrochemical cell using a bare ITO working electrode (black line) or ITO electrodes modified with **FP1**

6 (blue line) and **FP1**/CNC (red line) films. All films were obtained with 5 LS transfers. The electrolyte

7 medium contained 90 mM potassium phosphate at pH 7.0. The scan rate was 50 mV/s. Inset: magnification

8 of the potential window where the oxygen reduction reaction occurs.

9

10 **FP1**-functionalized ITO electrodes (Figure 7, blue trace) showed an overall drop of recorded

11 currents with respect to bare ITO, indicating a decrease in conductivity, pointing out the fullerene

12 insulating behavior [51]. In terms of faradaic processes, the comparison with bare ITO showed that

13 HER was still inhibited, while ORR was fully suppressed, as arisen from the disappearance of the

14 characteristic shoulder (see inset in Figure 7). This behavior was not surprising, considering that

15 fullerene films are not electroactive in aqueous environment in the potential range under

16 investigation. Fullerene reduction processes, whose nature is still debated, occur in fact at much

17 more negative potentials [78]. A strikingly different behavior arose in **FP1/CNC** composites (red

trace in Figure 7), which promoted a significant increase of cathodic currents. This finding suggested that CNCs facilitate the electron flow occurring at the hybrid film/electrolyte interface, improving the electrical conductivity and favoring the HER process. The shoulder related to ORR was absent (see inset in Figure 7), indicating again a hindering of the ORR process.

The justification of the observed behavior requires first an explanation on the origin of the HER process at our electrode surfaces. The protonated form of amines was shown by Cretu *et al*. [79,80] to act as a proton carrier, accelerating the hydrogen evolution reaction on different metal electrodes. This suggests that the ammonium pendants on the fullerene moieties of hybrid films promote the HER process, while lateral $-SO_{4-}$ groups of CNCs likely play a role in creating shuttling paths for protons from the bulk to the amine groups at the electrode surface, enhancing the faradaic cathodic current. Hence, the cooperative interaction between ammonium groups on fullerenes and sulphate groups on CNCs create the conditions for HER to take place efficiently.

Since fullerenes are known to be excellent photoactive materials, we preliminarily explored the photo-electrochemical activity of the assembled **FP1/**CNC hybrid films, in comparison to plain **FP1** films, in order to unveil the influence of CNCs on the photo-response of fullerene-based electrodes. Analogous LSV traces for ITO-**FP1** and ITO-**FP1**/CNC electrodes were recorded under illumination and compared with those obtained in dark conditions. Photoactivity arisen from the fullerene moiety was observed in both samples, although higher photocurrents were obtained in the case of **FP1**/CNC films. Notably, at the applied potential of -400 mV *vs* Ag/AgCl, the measured photocurrents were nearly 0.21 $\mu A/cm_2$ on ITO-**FP1** and nearly 0.75 $\mu A/cm_2$ on ITO-**FP1**/CNC, with a three-fold increment.

In agreement with LSV data photo-chronoamperometric traces recorded at -400 mV applied potential (Figure 8, panel B), confirmed that the presence of CNCs enhance the photo-response of the film, promoting the generation of a photocurrent at least twice as intense as that one recorded with the sole fullerene component. Both films showed fast electrical

response to the light stimulus with the attainment of a plateau photocurrent value and instant recovery of the background current upon switching off the lamp. Bare ITO electrodes showed a very poor photo-response (data not shown) in agreement with the key role of fullerene in the photo-sensitization of WE surface. Unlike what reported by Huang *et al*. [47], who evaluated the photo-response of LB films based on a fullerene dicarboxylic acid derivative in analogous experimental conditions, we could not suppress the photocurrent signal by removing dissolved oxygen with nitrogen. This finding further indicated that HER, rather than ORR, likely played a major role in photocurrent generation by our films. However, CNCs clearly acted as photocurrent enhancers on the photoactive fullerene-based material, an effect that was evident even in hybrid films prepared with a single transferred layer (see Figure S4). Therefore, CNCs proved to increase both background currents and photocurrents, indicating that the electron transfer processes sustaining the current under illumination were likewise favoured by the CNC-mediated assembly of C_{60} moieties. It is noteworthy that the amount of fulleropyrrolidine in **FP1**/CNC LS films was even lower than that one present in single-component **FP1** films, as arises from spectra in Figure S3, ruling out the attribution of the increased photoactivity to the photocatalyst amount. Thus, we can conclude that the nanocellulose partner highly improves the photo-electrocatalytic efficiency of cationic fulleropyrrolidines, by playing a role in the supramolecular organization of their films, by enhancing their two-dimensional and ionic character and by increasing wettability and electrical communication with the electrolyte medium.

1
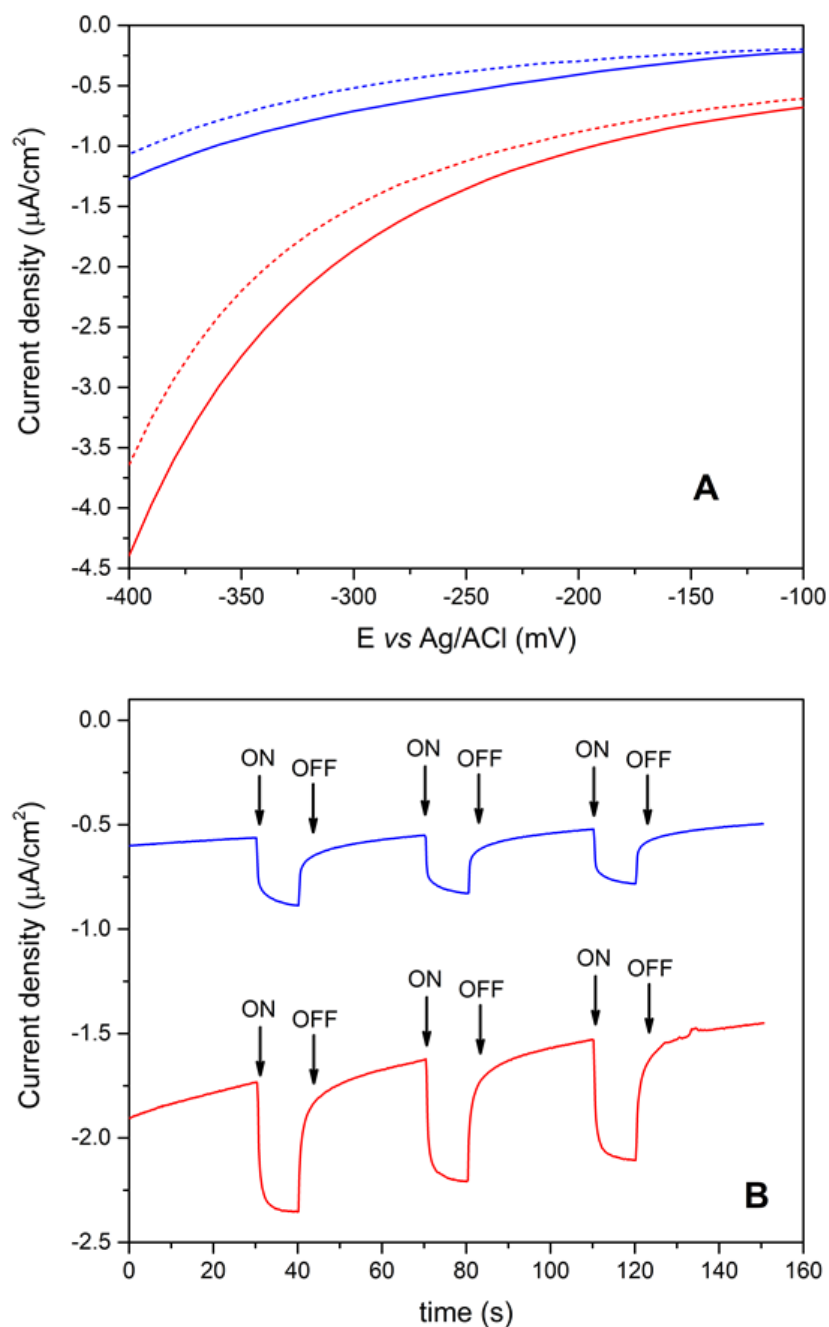
Figure 8. Panel A: LSV traces recorded under visible light illumination on ITO electrodes modified with **FP1** (blue continuous line) and **FP1**/CNC (red continuous line) films. LSV traces recorded in dark conditions are also reported for comparison (blue and red dashed lines for **FP1** and **FP1/CNC** films respectively). Scan rate was 50 mV/s. Panel B: Photo-chronoamperometry profiles recorded at -400 mV *vs* Ag/AgCl applied potential relevant to the same films of Panel A, namely plain **FP1** (blue line) and **FP1/CNC** (red line). The 10 s illumination period is indicated by arrows. All films were obtained with 5 horizontal transfers.

4. Conclusions

In this work, we have investigated the ability of anionic CNCs to assist the 2D-assembly of cationic fulleropyrrolidines at the air/water interface. The results of our investigation demonstrated that sulphated cellulose nanocrystals organize at the air-water interface, thanks to electrostatic interactions with the charged fullerene layer, affecting the enthalpy-driven assembly of fulleropyrrolidines during film compression, as indicated by modification of relevant Langmuir isotherms. In particular, the high aspect ratio of CNCs likely favours the binding of several fullerene units along the rod-shaped crystals, which consequently organize parallel to the interface. Moreover, it is reasonable to envisage that the rigid structure of CNCs plays a role in controlling the approaching of bound fullerene cages during lateral compression of the hybrid film, thus influencing intermolecular interactions among fullerenes in relevant LS films. The hybrid CNC/fullerene films can be transferred onto ITO/glass slides with a reproducible stoichiometry for both derivatives. The film homogeneity improves with multiple transfers in both cases, but the increase in molecular charge in **FP2** with respect to **FP1** induces a less efficient nanocellulose uptake from the water subphase into the transferred film. This could be ascribed either to the different molecular structure of **FP2,** in which the second positive charge close to the carbon cage could prevent an effective supramolecular interaction, or to the higher water solubility of the relevant supramolecular assemblies, responsible for their scarce adhesion and stability onto the solid support. Interestingly, during the self-assembly, fulleropyrrolidines loose a significant amount of trifluoroacetate counterion both on pure water and CNC subphases, pointing out amine deprotonation processes in absence of CNCs and a role of anionic nanocrystals in preservation of ammonium positive charges. The ammonium pendants proved to be involved in the enhancement of cathodic currents and photocurrents observed in **FP1/**CNC hybrid films deposited onto ITO electrodes with respect to CNC-free fullerene

layers. The high impact of CNCs on the (photo)electrochemical activity of **FP1** films revealed that CNCs are enhancers of the photo-electrocatalytic activity of fullerene-based coatings, by playing a multiple role in their two-dimensional supramolecular organization, in the preservation of their positive charge and in the increase of their overall wettability in the electrolyte medium.

Appendix A

Supplementary data related to this article can be found at https://doi.org/10.1016/j.carbon.2019.XXXX

References

[1] A. Dufresne, Nanocellulose: a new ageless bionanomaterial, Materials Today 16 (2013) 220-227.

[2] Y. Habibi, L.A. Lucia, O.J. Rojas, Cellulose nanocrystals: chemistry, self-assembly, and applications, Chem. Rev. 110 (2010) 3479-3500.

[3] D. Klemm, F. Kramer, S. Moritz, T. Lindström, M. Ankerfors, D. Gray et al., Nanocelluloses: a new family of nature-based materials, Angew. Chem. Int. Ed. 50 (2011) 5438-5466.

[4] M. Roman, Toxicity of cellulose nanocrystals: a review, Ind. Biotechnol. 11 (2015) 25-33.

[5] L. Colombo, L. Zoia, M.B. Violatto, S. Previdi, L. Talamini, L. Sitia et al., Distribution and bone tropism of cellulose nanocrystals in living mice, Biomacromolecules 16 (2015) 2862-2871.

[6] P. Zugenmaier, Conformation and packing of various crystalline cellulose fibers, Prog. Polym. Sci. 26 (2001) 1341-1417.

[7] S. Iwamoto, W. Kai, A. Isogai, T. Iwata, Elastic Modulus of Single Cellulose Microfibrils from Tunicate Measured by Atomic Force Microscopy, Biomacromolecules 10 (2009) 2571-2576.

[8] Nanocellulose and sustainability: production, properties, applications, and case studies, CRC Press, Taylor & Francis Group (2018).

[9] M. Nogi, S. Iwamoto, A.N. Nakagaito, H. Yano, Optically transparent nanofiber paper, Adv. Mater. 21 (2009) 1595-1598.

[10] M. Matsuo, C. Sawatari, Y. Iwai, F. Ozaki, Effect of orientation distribution and crystallinity on the measurement by x-ray diffraction of the crystal lattice moduli of cellulose I and II, Macromolecules 23 (1990) 3266-3275.

[11] T. Nishino, K. Takano, K. Nakamae, Elastic modulus of the crystalline regions of cellulose polymorphs, J. Polym. Sci. B Polym. Phys. 33 (1995) 1647-1651.

[12] J. Huang, P.R. Chang, Y. Chen, S. Gao, J. Liao, Fully Green Cellulose Nanocomposites, in: H. Kargarzadeh, I. Ahmad, S. Thomas, A. Dufresne (Eds.), Handbook of nanocellulose and cellulose nanocomposites, Wiley (2017).

[13] S. Bettini, S. Pal, S. Sawalha, A. Licciulli, L. Valli, G. Giancane et al., cellulose-based substrate for sers-promoted histamine picomolar detection in beverages, ChemistrySelect 4 (2019) 2968-2975.

[14] O.A. Battista, Hydrolysis and crystallization of cellulose, Ind. Eng. Chem. 42 (1950) 502-507.

[15] B.G. Rånby, Fibrous macromolecular systems. Cellulose and muscle. The colloidal properties of cellulose micelles, Discuss. Faraday Soc. 11 (1951) 158-164.

[16] Z.-Y. Wu, H.-W. Liang, L.-F. Chen, B.-C. Hu, S.-H. Yu, Bacterial cellulose: a robust platform for design of three dimensional carbon-based functional nanomaterials, Acc. Chem. Res. 49 (2016) 96-105.

[17] U.D. Hemraz, K. Ckless, Cellulose nanocrystals: a versatile nanoplatform for emerging biomedical applications AU - Sunasee, Rajesh, Expert Opin. Drug Del. 13 (2016) 1243-1256.

[18] N. Grishkewich, N. Mohammed, J. Tang, K.C. Tam, Recent advances in the application of cellulose nanocrystals, Curr. Opin. Colloid Interface Sci. 29 (2017) 32-45.

[19] H. Golmohammadi, E. Morales-Narváez, T. Naghdi, A. Merkoçi, Nanocellulose in sensing and biosensing, Chem. Mater. 29 (2017) 5426-5446.

[20] F. Brunetti, A. Operamolla, S. Castro-Hermosa, G. Lucarelli, V. Manca, G.M. Farinola et al., Printed solar cells and energy storage devices on paper substrates, Adv. Funct. Mater. 29 (2019) 1806798.

[21] A. Operamolla, Recent advances on renewable and biodegradable cellulose nanopaper substrates for transparent light-harvesting devices: interaction with humid environment, Int. J. Photoenergy 2019 (2019) 3057929 16 pages.

[22] TAPPI, Standard Terms and Their Definition for Cellulose Nanomaterials, TAPPI Standards: Regulations and Style Guidelines.

[23] J.F. Revol, H. Bradford, J. Giasson, R.H. Marchessault, D.G. Gray, Helicoidal self-ordering of cellulose microfibrils in aqueous suspension, Int. J. Biol. Macromol. 14 (1992) 170-172.

[24] R.H. Marchessault, F.F. Morehead, M.J. Koch, Some hydrodynamic properties of neutral suspensions of cellulose crystallites as related to size and shape, J. Coll. Sci. 16 (1961) 327-344.

[25] V.A. Zamolo, G. Modugno, E. Lubian, A. Cazzolaro, F. Mancin, L. Giotta et al., Selective targeting of proteins by hybrid polyoxometalates: interaction between a bis-biotinylated hybrid conjugate and avidin, Front. Chem. 6 (2018) 278.

[26] S. Bettini, Z. Syrgiannis, R. Pagano, L. Đorđević, L. Salvatore, M. Prato et al., Perylene bisimide aggregates as probes for subnanomolar discrimination of aromatic biogenic amines, ACS Appl. Mater. Inter. 11 (2019) 17079-17089.

[27] E.D. Cranston, D.G. Gray, Morphological and optical characterization of polyelectrolyte multilayers incorporating nanocrystalline cellulose, Biomacromolecules 7 (2006) 2522-2530.

[28] P. Podsiadlo, S.-Y. Choi, B. Shim, J. Lee, M. Cuddihy, N.A. Kotov, Molecularly engineered nanocomposites: Layer-by-Layer assembly of cellulose nanocrystals, Biomacromolecules 6 (2005) 2914-2918.

[29] A. Ulman, Introduction to Ultrathin Organic Films. From Langmuir-Blodgett to self-assembly, Elsevier 2013.

[30] M.G. Manera, E. Ferreiro-Vila, J.M. García-Martín, A. Cebollada, A. García-Martín, G. Giancane et al., Enhanced magneto-optical SPR platform for amine sensing based on Zn porphyrin dimers, Sensors Act. B: Chem. 182 (2013) 232-238.

[31] R. Rella, P. Siciliano, F. Quaranta, T. Primo, L. Valli, L. Schenetti et al., Gas sensing measurements and analysis of the optical properties of poly[3-(butylthio)thiophene] Langmuir–Blodgett films, Sensors Actuat. B: Chem. 68 (2000) 203-209.

[32] M.G. Manera, E. Ferreiro-Vila, A. Cebollada, J.M. Garcia-Martin, A. Garcia-Martin, G. Giancane, et al., Ethane-bridged Zn porphyrins dimers in Langmuir-Schafer thin films: spectroscopic, morphologic, and magneto-optical surface plasmon resonance characterization, J. Phys. Chem. C, 116 (2012) 10734-10742.

[33] L. Valli, G. Giancane, A. Mazzaglia, L.M. Scolaro, S. Conoci, S. Sortino, Photoresponsive multilayer films by assembling cationic amphiphilic cyclodextrins and anionic porphyrins at the air/water interface, J. Mater. Chem. 17 (2007) 1660-1663.

[34] S. Conoci, D.M. Guldi, S. Nardis, R. Paolesse, K. Kordatos, M. Prato et al., Langmuir–Shäfer transfer of fullerenes and porphyrins: formation, deposition, and application of versatile films, Chem-Eur. J. 10 (2004) 6523-6530.

[35] L. Valli, S. Casilli, L. Giotta, B. Pignataro, S. Conoci, V.V. Borovkov et al., Ethane-bridged zinc porphyrin dimers in Langmuir−Shäfer thin films: structural and spectroscopic properties, J. Phys. Chem. B 110 (2006) 4691-4698.

[36] Y. Habibi, L. Foulon, V. Aguié-Béghin, M. Molinari, R. Douillard, Langmuir–Blodgett films of cellulose nanocrystals: Preparation and characterization, J. Colloid Interf. Sci. 316 (2007) 388-397.

[37] Y. Habibi, I. Hoeger, S.S. Kelley, O.J. Rojas, Development of Langmuir−Schaeffer cellulose nanocrystal monolayers and their interfacial behaviors, Langmuir 26 (2010) 990-1001.

[38] A. Hajian, S.B. Lindström, T. Pettersson, M.M. Hamedi, L. Wågberg, Understanding the dispersive action of nanocellulose for carbon nanomaterials, Nano Lett. 17 (2017) 1439-1447.

[39] J. M. González-Domínguez, A. Ansón-Casaos, L. Grasa, L. Abenia, A. Salvador, E. Colom et al., Unique properties and behavior of nonmercerized type-ii cellulose nanocrystals as carbon nanotube biocompatible dispersants, Biomacromolecules 20 (2019) 3147−3160.

[40] H. Zheng, B. Ju, X. Wang, W. Wang, M. Li, Z. Tang et al. Circularly polarized luminescent carbon dot nanomaterials of helical superstructures for circularly polarized light detection, Adv. Optical Mater. 6 (2018) 1801246.

[41] L. Dai, D.W. Chang, J.-B. Baek, W. Lu, Carbon nanomaterials for advanced energy conversion and storage, Small 8 (2012) 1130-1166.

[42] V. Sgobba, G. Giancane, D. Cannoletta, A. Operamolla, O. Hassan Omar, G.M. Farinola, D.M. et al., Langmuir–Schaefer films for aligned carbon nanotubes functionalized with a conjugate polymer and photoelectrochemical response enhancement, ACS Appl. Mater. Inter. 6 (2014) 153-158.

[43] G. Giancane, A. Ruland, V. Sgobba, D. Manno, A. Serra, G.M. Farinola et al., Aligning single-walled carbon nanotubes by means of Langmuir–Blodgett film deposition: optical, morphological, and photo-electrochemical studies, Adv. Funct. Mater. 20 (2010) 2481-2488.

[44] V. Sgobba, G. Giancane, S. Conoci, S. Casilli, G. Ricciardi, D.M. Guldi et al., Growth and characterization of films containing fullerenes and water soluble porphyrins for solar energy conversion applications, J. Am. Chem. Soc. 129 (2007) 3148-3156.

[45] T. Da Ros, M. Prato, M. Carano, P. Ceroni, F. Paolucci, S. Roffia et al., Synthesis, electrochemistry, Langmuir–Blodgett deposition and photophysics of metal-coordinated fullerene–porphyrin dyads, J. Organomet. Chem. 599 (2000) 62-68.

[46] P.M. Allemand, A. Koch, F. Wudl, Y. Rubin, F. Diederich, M.M. Alvarez et al., Two different fullerenes have the same cyclic voltammetry, J. Am. Chem. Soc. 113 (1991) 1050-1051.

[47] N.S. Sariciftci, L. Smilowitz, A.J. Heeger, F. Wudl, Photoinduced electron transfer from a conducting polymer to buckminsterfullerene, Science 258 (1992) 1474.

[48] S. Günes, H. Neugebauer, N.S. Sariciftci, Conjugated polymer-based organic solar cells, Chem. Rev. 107 (2007) 1324-1338.

[49] Y. Huang, Y. Zhao, L. Gan, C.-H. Huang, N. Wu, Langmuir–Blodgett film formation of a fullerene dicarboxylic acid derivative C_{60}(HOOCCHNHCHCOOH) and its photocurrent generation, J. Colloid Interf. Sci. 204(2) (1998) 277-283.

[50] Y.A.J. Al-Hamadani, K.H. Chu, A. Son, J. Heo, N. Her, M. Jang e al, Stabilization and dispersion of carbon nanomaterials in aqueous solutions: A review, Sep. Purif. Technol. 156 (2015) 861-874.

[51] A. Szucs, A. Loix, J.B. Nagy, L. Lamberts, Fullerene film electrodes in aqueous solutions Part 1. Preparation and electrochemical characterization, J. Electroanal. Chem. 397 (1995) 191-203.

[52] L. Xiao, G.G. Wildgoose, R.G. Compton, Exploring the origins of the apparent "electrocatalysis" observed at C_{60} film-modified electrodes, Sensor Actuat. B Chem., 138 (2009) 524-531.

[53] L. Leo, G. Mele, G. Rosso, L. Valli, G. Vasapollo, D.M. Guldi et al., Interfacial properties of substituted fulleropyrrolidines on the water surface, Langmuir 16 (2000) 4599-4606.

[54] Y. Gao, Z. Tang, E. Watkins, J. Majewski, H.-L. Wang, Synthesis and characterization of amphiphilic fullerenes and their Langmuir−Blodgett films, Langmuir 21 (2005) 1416-1423.

[555] P. Bertoncello, A. Notargiacomo, V. Erokhin, C. Nicolini, Multi-walled carbon nanotubes (MWNTs) were functionalized via oxidative polymerization of 3-3′(vinylcarbazole), Nanotechnology 17 (2006) 699-705.

[56] H. Ding, M.K. Ram, L. Zheng, C. Nicolini, Fabrication and photovoltaic properties of fullerene and copper phthalocyanine derivative mixed Langmuir-Schaefer films, J. Mater. Sci. 36 (2001) 5423 – 5428.

[57] F. Fresno, R. Portela, S. Suárez, J.M. Coronado, Photocatalytic materials: recent achievements and near future trends, J. Mater. Chem. A 2 (2014) 2863-2884.

[58] D. Awfa, M. Ateia, M. Fujii, M. S. Johnson, C. Yoshimura, Photodegradation of pharmaceuticals and personal care products in water treatment using carbonaceous-TiO2 composites: A critical review of recent literature, Water Res. 142 (2018) 26-45.

[59] A.T. Najafabadi, Emerging applications of graphene and its derivatives in carbon capture and conversion: Current status and future prospects, Renew. Sust. Energ. Rev. 41 (2015) 1515-1545.

[60] L. Suhadolnik, A. Pohar, U. Novak, B. Likozar, A. Miheli, M. Čeh, Continuous photocatalytic, electrocatalytic and photo-electrocatalytic degradation of a reactive textile dye for wastewater-treatment processes: Batch, microreactor and scaled-up operation, J. Ind. Eng. Chem. 72 (2019) 178-188.

[61] L. Suhadolnik, A. Pohar, B. Likozarc, M. Čeh, Mechanism and kinetics of phenol photocatalytic, electrocatalytic and photoelectrocatalytic degradation in a TiO_2-nanotube fixed-bed microreactor, Chem. Eng. J. 303 (2016) 292-301.

[62] JH. Wu, Y. Huang, W. Ye, YG. Li, CO_2 Reduction: From the Electrochemical to Photochemical Approach, Adv. Sci. 4 (2017) 1700194.

[63] A. Herreros-López, M. Carini, T. Da Ros, T. Carofiglio, C. Marega, V. La Parola et al., Nanocrystalline cellulose-fullerene: Novel conjugates, Carbohydrate Polymers 164 (2017) 92–101.

[64] F. Awan, E. Bulger, R. M. Berry, K. C. Tam, Enhanced radical scavenging activity of polyhydroxylated C_{60} functionalized cellulose nanocrystals, Cellulose 23 (2016) 3589–3599.

[65] A. Operamolla, S. Casalini, D. Console, L. Capodieci, F. Di Benedetto, G.V. Bianco et al., Tailoring water stability of cellulose nanopaper by surface functionalization, Soft Matter 14 (2018) 7390-7400.

[66] K. Kordatos, T. Da Ros, S. Bosi, E. Vázquez, M. Bergamin, C. Cusan et al., Novel versatile fullerene synthons, J. Org. Chem. 66 (2001) 4915-4920.

[67] A. Serra, A. Genga, D. Manno, G. Micocci, T. Siciliano, A. Tepore et al., Synthesis and characterization of TiO_2 Nanocrystals prepared from n-octadecylamine−titanyl oxalate Langmuir−Blodgett films, Langmuir 19 (2003) 3486-3492.

[68] F. Italiano, A. Buccolieri, L. Giotta, A. Agostiano, L. Valli, F. Milano et al., Response of the carotenoidless mutant Rhodobacter sphaeroides growing cells to cobalt and nickel exposure, Int. Biodeter. Biodeg. 63 (2009) 948-957.

[69] A. N. Fernandes, L. H. Thomas, C. M. Altaner, P. Callow, V. T. Forsyth, D. C. Apperley et al., Nanostructure of cellulose microfibrils in spruce wood, Proc. Nat. Ac. Sci 108 (2011) E1195-E1203.

[70] T. Kondo, The assignment of IR absorption bands due to free hydroxyl groups in cellulose, Cellulose 4 (1997) 281.

[71] D. Ciolacu, F. Ciolacu, V. Popa, Amorphous cellulose - Structure and characterization, Cellulose Chem. Technol., 45 (2011) 13-21.

[72] M.L. Nelson, R.T. O'Connor, Relation of certain infrared bands to cellulose crystallinity and crystal latticed type. Part I. Spectra of lattice types I, II, III and of amorphous cellulose, J. Appl. Polym. Sci. 8 (1964) 1311-1324.

[73] G. Socrates, Infrared characteristic group frequencies: tables and charts, 3rd ed. (2001) Chichester, West Sussex, John Wiley & Sons.

[74] W. Klemperer, G.C. Pimentel, Hydrogen bonding in sodium trifluoroacetate-trifluoroacetic acid compounds, J. Chem. Phys. 22 (1954) 1399-1402.

[75] H. Wang, X. Zhao, K.B. Eisenthal. Effects of monolayer density and bulk ionic strength on acid−base equilibria at the air/water interface, J. Phys. Chem. B 104 (2000) 8855-8861.

[76] C. Chen, L. Hu, Nanocellulose toward advanced energy storage devices: structure and electrochemistry, Acc. Chem. Res. 51 (2018) 3154−3165.

[77] A. Vargas-Uscategui, E. Mosquera, B. Chornik, L. Cifuentes. Electrocatalysis of the hydrogen evolution reaction by rhenium oxides electrodeposited by pulsed-current, Electrochim. Acta 178 (2015) 739–747.

[78] L. Xiao, G.G. Wildgoose, A. Crossley, R.G. Compton, The electroreduction of "C_{60}" films in aqueous electrolyte does not lead to alkali metal ion insertion—Evidence for the involvement of adventitious poly-epoxidated C_{60} ($C_{60}O_n$), Sensor and Actuat B: Chem. 138 (2009) 397-401.

[79] R. Creţu, A. Kellenberger, M. Medeleanu, N. Vaszilcsin, Cathodic hydrogen evolution reaction on gold catalyzed by proton-carriers. Int. J. Electrochem. Sci., 9 (2014) 4465 – 4477.

[80] R. Creţu, A. Kellenberger, N. Vaszilcsin, Enhancement of hydrogen evolution reaction on platinum cathode by proton carriers, Int. J. Hydrogen Energ 38 (2013), 11685-11694.